Research article

Synthesis of Co@CoO/C by micro-tube method and their electrochemical performances

Jun Du [a,b], Binbin Jin [a,b], Lang Liu [a,b], Ling Chen [a,b], Xing Fan [a,b], Bingxin Lei [a,b], Liying Liang [a,b,c,*]

[a] *School of Materials and Environment, Guangxi Minzu University, Nanning, 530000, PR China*
[b] *Guangxi Colleges and Universities Key Laboratory of Environmental-Friendly Materials and Ecological Remediation, Guangxi Key Laboratory of Advanced Structural Materials and Carbon Neutralization, School of Materials and Environment, Guangxi Minzu University, Nanning, 530105, PR China*
[c] *Guangxi Research Institute of Chemical Industry Co., Ltd, Nanning, 530001, PR China*

A B S T R A C T

Lithium-ion batteries (LIBs) are promising secondary batteries that are widely used in portable electronic devices, electric vehicles and smart grids. The design and synthesis of high-performance electrode materials play a crucial role in achieving lithium-ion batteries with high energy density, prolonged cycle life, and superior safety. CoO has attracted significant attention as a negative electrode material for lithium-ion batteries due to its high theoretical capacity and abundant resources. However, its limited conductivity and suboptimal cycling performance impede its potential applications. The study proposes a novel micro-tube reaction method for the synthesis of Co@CoO/C, utilizing Kapok fiber as a template with a special hollow structure. The microstructure and composition of the samples were characterized using X-ray powder diffraction (XRD), X-ray photoelectron spectroscopy (XPS), scanning electron microscopy (SEM) and transmission electron microscopy (TEM). After conducting electrochemical performance tests, it was discovered that at a current density of 100 mA/g and within the range of 0.01–3.0 V for 50 charge and discharge cycles. Co@CoO/C composite negative electrode exhibits a reversible lithium insertion specific capacity of 499.8 mAh/g and keep a discharge capacity retention rate of 97.6 %. The greatly improved lithium storage and stability performance of Co@CoO/C composite anode is mainly attributed to the synergistic effect between Co@CoO nanoparticles and the kapok carbon microtubule structure.

1. Introduction

Lithium-ion batteries (LIBs) are extensively utilized in mobile electronic devices and electric vehicles due to their unparalleled performance compared to other conventional secondary batteries [1–5]. Negative electrode materials, as an indispensable component of lithium-ion batteries, have been the primary focus of research. The conventional theoretical specific capacity of graphite anode materials is reported to be 372 mAh/g [5–7], no longer suffices to meet the burgeoning demand for high-capacity and high-performance batteries. High theoretical specific capacity (712 mAh/g) and abundant resources make CoO as an excellent

---

alternative to graphite materials. However, CoO has poor electrical conductivity, and undergoes a huge volume expansion effect during the charge and discharge process, which leads to the structural damage of electrode materials, powders and falls off, and then affects the cycle stability of the battery [8–10], limiting its commercial application in LIBs.

In order to solve these problems, numerous researchers have invested a lot of time and effort towards their resolution. Two main approaches have been reported: one approach is to shrink CoO particles to nanometer size and build special nanostructures such as nanofibers [11], nanoparticles [12], nanosheets [13], and nanotubes [14]. The special nanostructures of CoO can help to improve the electrochemical performance by reducing the bulk strain of oxide particles during lithium embedding and extraction and enhancing their resistance to comminution [15]. Furthermore, the introduction of carbon-containing materials such as carbon nanofibers [16], graphene [13] and carbon nanotubes [17] into CoO also has been reported. Carbon materials not only improve the electrical conductivity of the material, but also have a buffering effect on the volume expansion of CoO during charging and discharging [18–20]. However, the synthesis process of these carbon carriers is complicated and costly, making it difficult to use them on a large scale. Currently, the primary techniques utilized for synthesizing CoO electrode materials include hydrothermal synthesis [21], ammonia-assisted synthesis [5,22], electrospinning [23] and other related methodologies. Although these methods can be utilized to prepare nanostructures with diverse morphologies, they all possess certain limitations such as intricate synthesis procedures, challenging operations and controls, which ultimately increase the cost of fabricating CoO electrode materials.

In recent years, materials researchers have turned their attention to the unique functional characteristics, diverse morphology and structure of biological materials in nature. The special natural structures of plants, animals, and microorganisms are now being directly harnessed as "biological templates" to synthesize a range of novel materials while retaining their chemical composition and morphology [24–26]. The biological hard carbon is one of the most promising negative electrodes due to its economy, sustainability and rich natural structure. Carbon-containing materials made from bamboo [27], grain hulls [28], wood [29] and tea leaves [30] have proven to be excellent electrode materials for LIBs applications. Moreover, we have observed the presence of microtubular structures in kapok materials which possess a number of advantageous characteristics including renewability, eco-friendliness, high carbon content, huge specific surface area and porosity [31]. When microtubules are in contact with a liquid surface, an observable capillary phenomenon occurs, which can be used for the synthesis of new materials [24].

This study presents a novel approach, termed the 'micro-tube reaction method', for synthesizing Co@CoO/C composites based on the principles of a biological template and the capillarity phenomenon. Kapok fiber with a microtubular structure was chosen as both the carbon source and template. The capillary effect facilitated the absorption of CoO precursor solution into plant microtubules for reaction, resulting in the formation of Co@CoO/C composite through carbothermal reduction process. Its electrochemical properties were subsequently investigated.

2. Materials and methods

2.1. Laboratory equipment

OTF-1200X-S High temperature tube atmosphere furnace was used for firing samples (Hefei Kejing Material Technology Co., LTD.). The materials were characterized using an XRD diffractometer (Bruker, Germany), S-4700 scanning electron microscope (Hitachi, Japan), field emission transmission electron microscope (Philip-FEI, Netherlands), and high-performance imaging X-ray photoelectron spectrometer (Shimazu-Kratos, Japan). Other equipment included the Super purification glove box (Mikrouna); Land CT2001A battery test system (Wuhan Landian Electronics Co., LTD.). $Co(NO_3)_2 \cdot 6H_2O$, ethanol, and ammonia were all pure analytical reagents manufactured by Sinopharm Chemical Reagent Co., Ltd. for laboratory use.

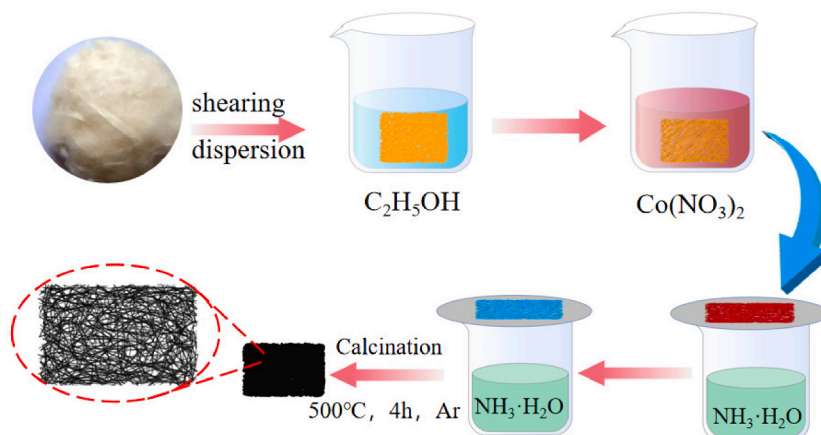**Fig. 1.** Schematic illustration of the Co/(CoO)/C composite materials.

2.2. Experimental procedure

A 5 g $Co(NO_3)_2 \cdot 6H_2O$ crystal was dissolved in 5 mL deionized water. The kapok fiber was subsequently cleaned, dried and cut into small sections with a growth degree of approximately 2–3 mm. It was then dispersed in anhydrous ethanol. After the kapok had been evenly dispersed, the Kapok fiber was extracted from anhydrous ethanol, drained of surface liquid, and subsequently immersed in a prepared solution of $Co(NO_3)_2$. Once the kapok fiber has achieved a homogeneous pink color, it should be extracted and drained of any superficial liquid prior to its placement atop concentrated ammonia water. The $Co(NO_3)_2$ within the kapok fiber underwent a reaction with ammonia gas through diffusion, resulting in the formation of a blue-green coloration. The reaction must be promptly terminated at this point in order to acquire cobalt hydroxide/carbon precursor.

The cobalt hydroxide/carbon precursor was loaded into a graphite boat, which was subsequently sealed and placed inside a tube furnace. Under the protection of 60 sccm argon gas, heat up at a rate of 5 °C/min until reaching 500 °C and maintain this temperature for 2 h. After being cooled to room temperature in the furnace, the final product Co@CoO/C composite was obtained through grinding and dispersing processes. Furthermore, a comparative sample of Kapok fiber-derived carbon was synthesized using identical heat treatment conditions, as illustrated in Fig. 1.

The sample to be tested, Super P Li conductive carbon black (super high density), PVDF (Arkema polyvinylidene fluoride binder HSV900 type) were mixed according to the mass ratio of 85 %: 10 %: 5 %. The mixture was mixed with N-methyl pyrrolidone, stirred until it reached a thick consistency, coated onto copper foil, dried under vacuum (−0.1 MPa) at 60 °C for 6 h, cooled and cut into discs about 1 cm in diameter. The half battery was assembled in the glove box (Michelina) with a CR2016 button battery. The utilized diaphragm was made of Celgard 2400 polypropylene diaphragm. The electrolyte consists of a 1 M LiPF6 mixed solution comprising ethylene carbonate (EC) and diethyl carbonate (DEC), with an equal volume ratio of 1:1 for EC and DEC. The negative electrode consisted of a commercially available circular lithium sheet with a diameter of 1.5 cm, and ensure that the load of active substances is between 0.8 and 1.2 mg/cm^2. The electrochemical charging-discharging performance was evaluated by Land CT2001A battery test system (Wuhan Landian Electronics Co., LTD.).

3. Results and discussions

3.1. Structural analysis

The SEM images of the sample material which was calcined for 2 h under argon atmosphere protection at 500 °C are shown in Fig. 2a, b. As depicted in Fig. 2a, the hollow tubular structure and morphology of Kapok fiber remained well-preserved after calcination, exhibiting an approximate diameter of 10 μm. Additionally, a layer of granular material was uniformly deposited onto the inner surface of the tube wall. Upon further magnification (Fig. 2b), it became evident that the particle size ranged from 2 to 200 nm. The XRD pattern of the synthesized sample is displayed in Fig. 2c, exhibiting four characteristic peaks. By comparing with the standard card (JCPDF no.43-1004), it can be observed that the diffraction peaks at 36.5°, 42.4° and 61.5° correspond to the crystal planes (111), (200) and (220) of cubic CoO (Fm3m), respectively. The diffraction peak observed at 44.2° corresponded to the (111) crystal face of cubic Co (Fm3m), as determined by comparison with the standard card (JCPDF no.15-0806) [32]. This indicates that the sample, prepared by calcination for 2 h under the protection of argon atmosphere at 500 °C, contains both CoO and Co, thus confirming its composition as a Co@CoO/C composite material.
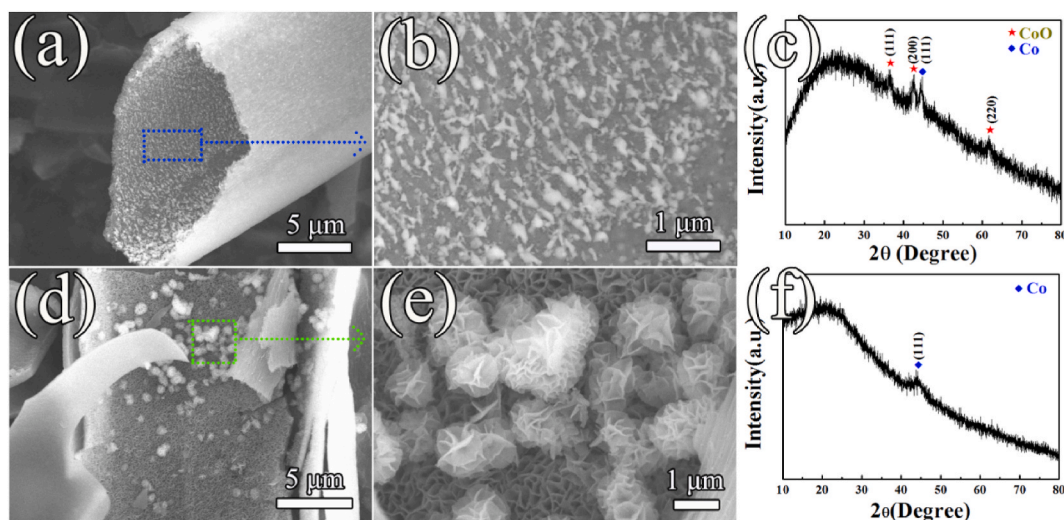

Fig. 2. (a, b) SEM images of the sample synthesized at 500 °C for 2 h; **(c)** XRD patterns of as-prepared samples synthesized at 500 °C for 2 h; **(d, e)** SEM images of the sample synthesized at 500 °C for 4 h; **(f)** XRD patterns of as-prepared samples synthesized at 500 °C for 4 h.

The SEM images of the sample material calcined for 4 h under argon atmosphere protection at 500 °C are presented in Fig. 2d, e. The hollow tubular structure and morphology of Kapok fiber can be effectively maintained after calcination, as demonstrated in Fig. 2d, where a layer of flake material was uniformly and densely distributed on the tube wall surface. This distribution was significantly denser compared to the sample prepared after a 2 h calcination (Fig. 2a). Upon further magnification (Fig. 2e), it became evident that the lamellar structures were distributed uniformly, creating porous formations with pore sizes ranging from 50 nm to 150 nm. Additionally, some of these lamellar structures coalesced into flower-like shapes. The XRD pattern of the prepared sample in Fig. 2f exhibited a distinct diffraction peak at 44.2°, which corresponds to the (111) crystal face of cubic Co (Fm3m), as confirmed by comparison with standard card JCPDF no.15-0806 [32]. The results indicate that the sample, which was subjected to calcination for 4 h under argon atmosphere protection at 500 °C, was exclusively composed of Co and lacked CoO, thus qualifying as a Co/C composite material.

The variation under argon atmosphere protection at 500 °C in the calcination time resulted in differences in the composition of the final sample. The reason behind this phenomenon is that the $Co(OH)_2$ generated by the microtubule reaction decomposes after heating in the precursor body and produced CoO (reaction equation (1)). With the increase of holding time, Kapok fiber undergone gradual carbonization, and CoO is then restored by carbon atoms to form nano Co particles (reaction equation (2)) [33,34].

$$Co(OH)_2 \rightarrow CoO + H_2O \qquad\qquad\qquad 1$$

$$2\,CoO + C \rightarrow 2\,Co + CO_2 \qquad\qquad\qquad 2$$
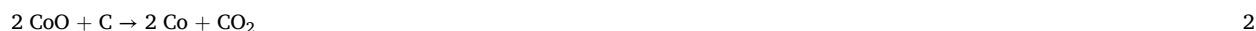
The low-power TEM image of calcination for 2 h under argon atmosphere protection at 500 °C is shown in Fig. 3a. The flake structure in the figure was the morphology of the sample after grinding. The Co@CoO/C composite tubular structure was disrupted during grinding, but its properties will remain unaffected. The kapok fiber can still serve as a template and carbon source, ensuring the secure immobilization of the Co@CoO particles in the tube wall. The HRTEM image of (Fig. 3a) is shown in Fig. 3b, revealing distinct lattice fringe images. The lattice fringes of 2.5 nm and 2.0 nm correspond to the (111) crystal faces of CoO and Co, respectively, which is consistent with Fig. 2c [35]. The low-power TEM images of calcination for 4 h under argon atmosphere protection at 500 °C is shown in Fig. 3c, revealing the flake structure morphology of the sample after grinding. After grinding, the tubular structure of Co/C composite material was destroyed, but its performance remained unaffected. Moreover, Kapok fiber still effectively plays the role of a template and carbon source, facilitating the immobilization of Co particles within the tube walls. Fig. 3d is the HRTEM image of Fig. 3c which reveals the presence of Co particles and crystal lattice fringe images in specific regions, thereby indicating that the Co particles were embedded within the carbon matrix with high crystallinity. The lattice spacing of Co particles, which measuring 2.0 nm, was
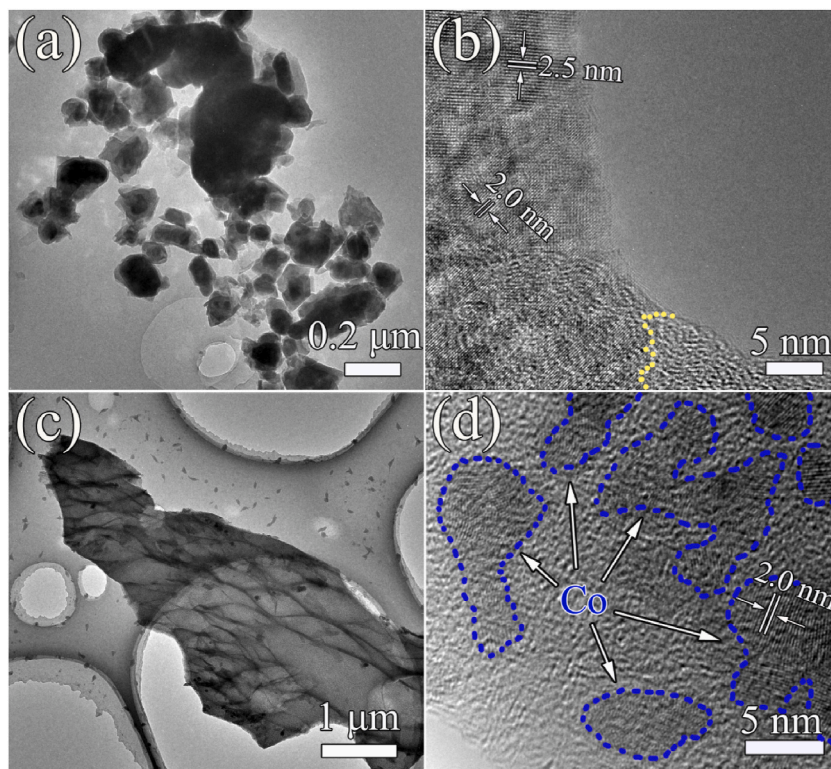
Fig. 3. (**a**) TEM image of Co@CoO/C sample; (**b**) HRTEM image of Co@CoO/C sample; (**c**) TEM image of Co/C sample; (**d**) HRTEM image of Co/C sample.

found to be in accordance with the (111) crystal face of cubic phase Co. This result indicates that the obtained Co particles exhibit a distinct (111) crystal face, which was in accordance with the strongest peak observed in Fig. 2f of the XRD analysis [36].

To determine the chemical composition of the synthesis material surface, X-ray photoelectron spectroscopy (XPS) tests were performed on Co@CoO/C. The complete spectral line scan, as shown in Fig. 4a, exhibited three distinct peaks specifically corresponding to the elements Co, C, and O with their primary and secondary peaks. The energy spectra of C 1s, O 1s and Co 2p corresponded to the observed main peaks, respectively, indicating the presence of three elements of Co, C and O on the surface of Co@CoO/C composite. To achieve a more precise analysis of the energy spectra for these six elements, the primary spectra of each elements were individually scanned. The Co 2p peak is illustrated in Fig. 4b. It was evident that the Co 2p peak exhibited two distinct peaks, namely $2p_{3/2}$ and $2p_{1/2}$, accompanied by corresponding satellite peaks adjacent to the primary peak. The peaks observed at 777.9 eV and 793.4 eV correspond to the Co $2p_{3/2}$ and Co $2p_{1/2}$ orbitals, respectively, with a separation of 15.5 eV, indicating the presence of CoO state in the Co@CoO/C composite, thereby providing further evidence for the existence of CoO. The C 1s spectrum of the Co@CoO/C composite, as illustrated in Fig. 4c, was successfully deconvoluted through curve fitting analysis. Each peak exhibited a four-component fit, indicating the presence of carbon in distinct binding modes on the surface of the Co@CoO/C composite. The C 1s peak at 284.7 eV corresponded to the C–C bond [37], while the peak at 285.7 eV was attributed to the C–H bond [38]. The peak observed at 287.9 eV can be attributed to the presence of a carbonyl group (C=O) [39], and finally, a distinct peak appeared at 289 eV corresponding to the O–C=O functional group [40]. The presence of four peaks in the O 1s spectrum depicts in Fig. 4d indicate that oxygen exists in four distinct states, with a binding energy of 530 eV corresponding to O–Co. The binding energies of 531.4 eV, 532.3 eV, and 533.6 eV corresponded to the O–H bond [41], the O–C bond [42] and the O–C=O bond [43], respectively.

3.2. Electrochemical performance test

The electrochemical performance curves of Co@CoO/C composites are shown in Fig. 5. The discharge/charge voltage profiles of Co@CoO/C composite anode at a 100 mA/g current density for the 1st, 2nd, 3rd, 10th, 20th, and 50th cycles are shown in Fig. 5a (0.01–3.0 V vs. Li^+/Li). The Co@CoO/C composite anode exhibited initial discharge and charge capacities of 733 mAh/g and 522 mAh/g, with an initial coulombic efficiency of 71.25 %. In the initial cycles, a significant capacity loss was primarily observed due to the formation of solid electrolyte interface (SEI) films and inert Li_2O, resulting in irreversibility. In the first discharge curve, a single plateau is observed at 0.7 V, which corresponds to the reduction of CoO to cobalt metal and the formation of a large amount of SEI film (reaction equation (3)) [44]. In the 2nd and 3rd discharge curves, a voltage plateau of 1.2–1.4 V is observed, which may be attributed to the formation of a small amount of SEI film and the reduction of Co_2O_3 to cobalt metal (reaction equation (4)). And in the 10th, 20th, and 50th discharge curves, we can observe a significant decrease in the voltage plateau of 1.0–1.2 V, which is due to the reduction of Co_2O_3 to metallic cobalt (reaction equation (4)) [45]. In the charging curves, the voltage plateaus of the negative electrodes of Co@CoO/C composites are all around 2.0 V, which is mainly attributed to the reoxidation of metallic Co(reaction equation (5)). However, the voltage plateaus of the first discharge curves are lower than those of the subsequent discharge curves, which may be attributed to the decomposition of part of the SEI.
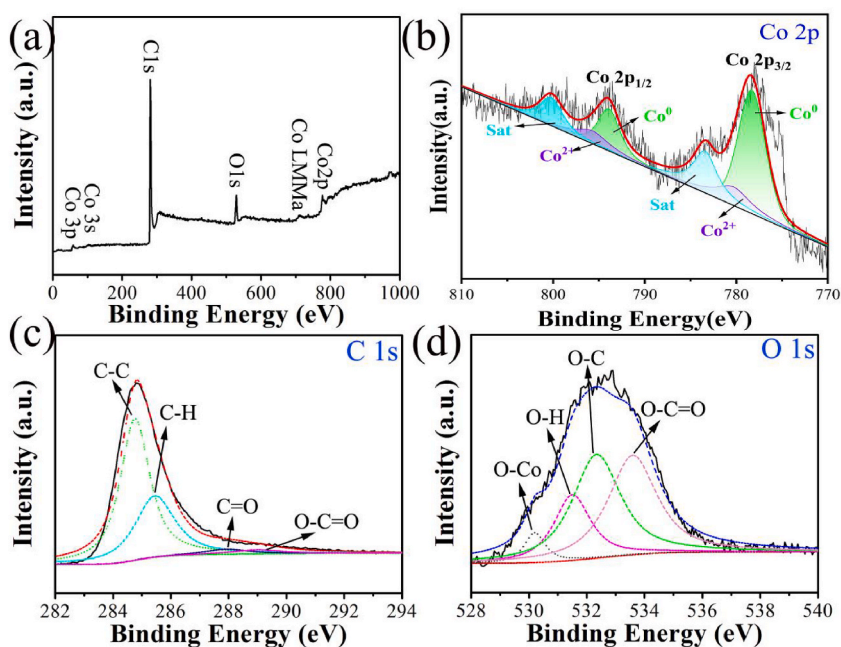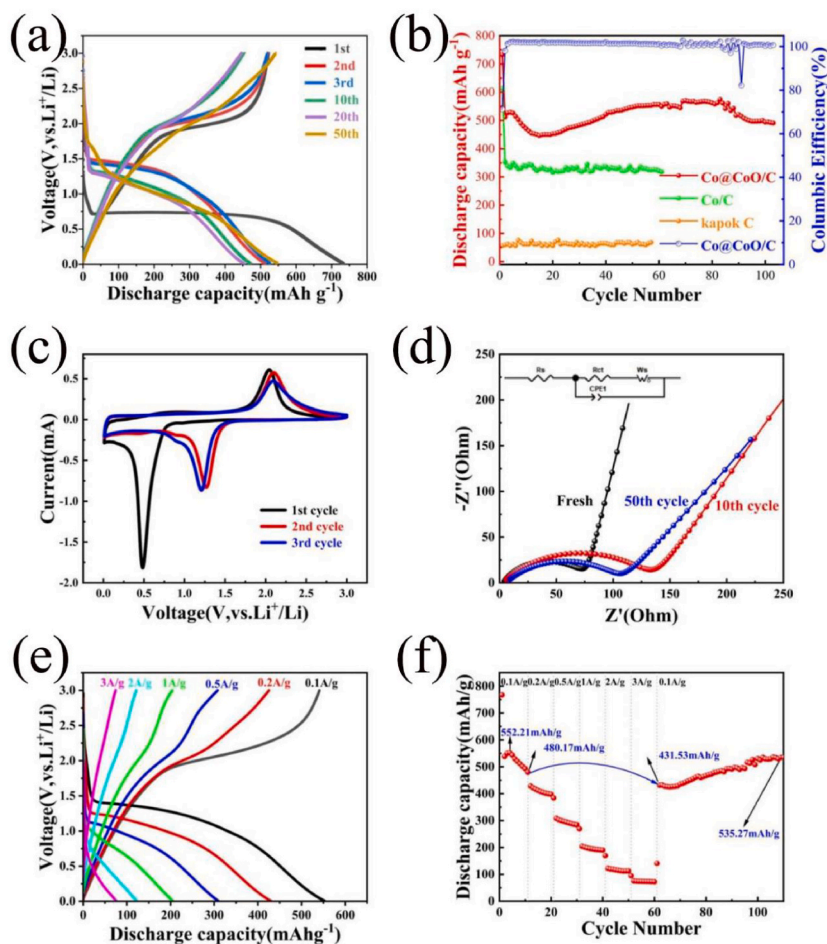

Fig. 4. The survey pattern of the surface binding energy of the Co@CoO/C. (**a**) Survey spectrum and high-resolution; (**b**) Co 2p; (**c**) C 1s; (**d**) O 1s.

Fig. 5. (**a**) Charge/discharge profiles of Co@CoO/C anode; (**b**) cycling performance and coulombic efficiency of Co@CoO/C electrodes; (**c**) CV curves of Co@CoO/C composite anode in different cycles; (**d**) Nyquist plots and equivalent circuit diagrams of Co@CoO/C composite anode after different cycles; (**e**) charge/discharge profiles of Co@CoO/C anode at various current densities; (**f**) rate and cycling performances of Co@CoO/C composite anode.

$$CoO + 2Li^+ + 2e^- \rightarrow Co + Li_2O \qquad\qquad 3$$

$$3Co + 4Li_2O \rightarrow Co_3O_4 + 8Li^+ + 8e^- \qquad\qquad 4$$

$$Co_3O_4 + 8Li^+ + 8e^- \rightarrow 3Co + 4Li_2O \qquad\qquad 5$$

The long-cycle performance and Coulombic efficiency plots of the Co@CoO/C, Co/C and kapok carbon composite anode at a current density of 100 mA g^{-1} are shown in Fig. 5b. It is obvious that the capacity of Co@CoO/C composite anode exhibits a decreasing trend in the first 15 cycles, which is mainly due to the fact that the pristine Co particles can activate and promote the reversible decomposition and formation of some SEI components in the first 15 cycles, which results in the loss of capacity. Until the pristine Co particles have completely reacted and formed a stable SEI film, and with the complete lithiation of CoO particles, the capacity significant increased [12]. The Co@CoO/C composite anode achieved a high reversible specific capacity of 499.8 mAh/g after 100 cycles, accounting for 97.6 % of the second cycle's capacity (512 mAh/g). In contrast, the Co/C and kapok C composite anodes exhibit reversible capacities of only 329 and 67 mAh/g after another 50 cycles. The stable cycling performance and reversible specific capacity of Co@CoO/C composite anodes are significantly higher than those of current carbon-based anode materials. Apparently, the combination of the unique microtubular structure of the kapok carbon matrix and the CoO nanoparticles significantly enhance its electrochemical performance. The Co@CoO/C composite anode exhibits exceptional capacity retention due to its unique microtubular composite structure, which effectively accommodates the volume changes associated with Li$^+$ insertion/extraction. On the other hand, a high specific surface area can enhance the contact of CoO nanoparticles with lithium ions, while the carbon matrix can improve material conductivity and reduce the diffusion distance of Li$^+$.

As shown in Fig. 5c, the first three CV curves of the Co@CoO/C composite negative electrode are presented within the voltage range of 0.01 and 3.0 V at a scan rate of 0.1 mV s^{-1}. In agreement with a large number of literature reports, the CV curves of the first cycle were completely different from those of the subsequent cycles, especially for the discharge process. During the initial cathodic polarization cycle, two distinct cathodic peaks (relative to Li$^+$/Li) were observed at 0.5 and 1.0 V, primarily attributed to the formation of a solid electrolyte interphase (SEI) at the electrode interfaces and surfaces, as well as the lithiation reaction of CoO (reaction equation (3)). During anodic polarization, an anodic broad peak was recorded in the range of 2.0–2.3 V, corresponding to a complex phase transition from Co^0 to Co^{2+} and Co^{3+}(reaction equation (4)). In contrast, a distinct cathodic peak emerged at 1.25 V after the second cycle, accompanied by a significant decrease in its intensity. This observation suggests that the formation of the SEI film leads to multiple irreversible reactions, which ultimately contributed to the capacity loss of the anode material during the initial cycle. However, it is noteworthy that the CV curves exhibited nearly identical profiles after the initial cycle, suggesting the formation of a robust SEI film on both the surface and interface of the carbon shell during the first cycle. This SEI film effectively prevented direct contact between CoO nanoparticles and the electrolyte, thereby safeguarding the structural integrity of internal CoO during subsequent charge/discharge cycles. Consequently, this protective mechanism contributed to a high Coulombic efficiency and ensured the excellent reversibility and stability of the sample.

In order to further investigate the excellent electrochemical performance of the Co@CoO/C anode, electrochemical impedance spectroscopy (EIS) was conducted in the frequency range of 0.01 Hz–100 KHz with the aim of establishing a correlation between electrode kinetics and electrochemical performance. Nyquist plots and equivalent circuit diagrams of Co@CoO/C composite anode are shown in Fig. 5d. The EIS plot consists of a circular arc and a straight line. The intercept at the real axis is attributed to the electrolyte resistance Rs, while the charge transfer resistance Rct of the electrode is determined by the size of the semicircle in the mid-frequency region, and the low-frequency tilted line is related to the diffusion coefficient of Li$^+$ in the electrode material. The new Co@CoO/C negative electrode showed a remarkable interfacial resistance of 71 Ω. This resistance then increases to 135 Ω after 10 cycles and gradually decreases to 103 Ω after 50 cycles. This is mainly due to the fact that the electrode material continues to be activated with an increasing number of cycles, resulting in improved reaction kinetics. The AC impedance measurements were consistent with the cycling performance, as shown in Fig. 5b.

The rate capacity was investigated at various current densities in order to further evaluate the electrochemical performance of Co@CoO/C. The charge/discharge curves and the multiplicity and cycling performance of the Co@CoO/C anode at different current densities are shown in Fig. 5e,f. The electrode exhibited a reversible capacity of 480.2 mAh/g when first cycled at 100 mA/g for 10 times. When the charge/discharge current density was increased to 200, 500, 1000, 2000, and 3000 mA/g, the reversible capacity of the Co@CoO/C negative electrode remained at 428.9, 308.7, 204.7, 119.9, and 94.9 mAh/g, respectively. In addition, when the current rate eventually returned to its initial value of 100 mA/g, the discharge capacity of the 60th cycle (431.5 mAh/g) was 89.9 % relative to the discharge capacity of the 10th cycle (480.2 mAh/g). After 100 cycles, the specific capacity increased to a value of 535.27 mAh/g, which was consistent with the cycling performance shown in Fig. 5b. The results indicate that the structure of the Co@CoO/C anode remained stable under high rate charge/discharge cycling conditions. The enhanced electrochemical performance can be attributed to the synergistic effect between the kapok carbon microtubule structure, which facilitates surface contact with CoO. Moreover, carbon exhibits a remarkable Li storage capacity and possesses high electronic conductivity, thereby facilitating the electrical connectivity of CoO nanoparticles and effectively stabilizing them against agglomeration during charging/discharging processes.

The above experimental data demonstrates the exceptional cycling stability and excellent multiplicity performance of the Co@CoO/C composite anode. Due to the poor electronic conductivity and large volume change of original CoO material during the repetitive lithiation/delithiation reaction, it caused a significant initial capacity loss, poor cycling stability, as well as very low multiplicity performance. In contrast, in Co@CoO/C composites, kapok carbon serves as the microtubule matrix structure for Co@CoO nanoparticles, which are encapsulated both internally and externally within the microtubules. During the charging and discharging process, the microtubule structure can provide sufficient space to accommodate the volumetric strain induced by lithium delithiation of Co@CoO embedded within lithium. This helps mitigate degradation of the SEI membrane, prevent capacity loss, and enhance cycling stability. Moreover, the kapok carbon matrix can shorten the migration path of lithium ions, increase the diffusion coefficient of lithium ions, and improve the electrical conductivity of Co@CoO/C composites. Therefore, the incorporation of Co@CoO nanoparticles and kapok carbon synergistically enhances the lithium storage performance and significantly improved the stability of the Co@CoO/C composite anode.

4. Conclusions

In this study, Co@CoO/C composite electrode materials were successfully synthesized using a simple, convenient and economical microtubule reaction method using cottonwood fiber as a template and carbon source. The chemical composition of Co@CoO/C was adjusted by controlling the holding time. At a current density of 100 mA/g, the Co@CoO/C composite negative electrode maintained a discharge capacity of 499.8 mAh/g and retained 97.6 % of its discharge capacity after 100 cycles (According to Yuan et al. reported that their prepared CoO/C material maintained a reversible capacity of 510 mAh/g after 50 cycles at a current density of 100 mA/g [22]). And after 3 A/g high current density cycling, it still has a discharge capacity of 535.27 mAh/g after 50 turns of 100 mA/g cycling. The excellent cycling stability and electrochemical performance can be attributed to the synergistic effect of the kapok template and CoO nanoparticles, which provide a microtubular carbon skeleton structure that prevents the agglomeration of the CoO nanoparticles and improves the electrical conductivity of the metal oxide. Moreover, the microtubule skeleton provides large sufficient space to alleviate the volumetric strain caused by the embedding/embedding of CoO nanoparticles with lithium ions. The Co@CoO/C

composite anode materials prepared in this study are green, low-cost and easy to synthesize. Together with their excellent electrochemical properties, they have the possibility for large-scale production, and a broad application prospect in high-performance lithium-ion battery anodes.

Funding

Data availability statement

Data will be made available on request.

CRediT authorship contribution statement

Jun Du: Writing – review & editing, Supervision, Project administration, Funding acquisition. **Binbin Jin:** Writing – original draft, Resources, Data curation. **Lang Liu:** Writing – review & editing, Validation. **Ling Chen:** Writing – review & editing, Formal analysis. **Xing Fan:** Writing – review & editing, Software, Resources, Methodology. **Bingxin Lei:** Writing – review & editing, Validation, Supervision. **Liying Liang:** Writing – review & editing, Visualization, Funding acquisition.

Declaration of competing interest

The authors declare that they have no known competing financial interests or personal relationships that could have appeared to influence the work reported in this paper.

References

[1] Y. Liu, J. Li, B. Liu, Y. Chen, Y. Wu, X. Hu, G. Zhong, J. Yuan, J. Chen, H. Zhan, Z. Wen, Confined WS2 nanosheets tubular nanohybrid as high-kinetic and durable anode for sodium-based dual ion batteries, ChemSusChem 16 (2023) e202201200, https://doi.org/10.1002/cssc.202201200.

[2] H. Xing, Y. Niu, J. Wang, Y. Liu, X. Yao, Y. Xu, Embedding cobalt (II, III) oxide nanoparticles into nitrogen-doped carbon nanotubes-grafted hollow polyhedrons as sulfur hosts for ultralong-life lithium-sulfur batteries, J. Colloid Interface Sci. 649 (2023) 832–843, https://doi.org/10.1016/j.jcis.2023.06.146.

[3] C. Wang, Y. Chen, D. Su, W.-L. Man, K.-C. Lau, L. Han, L. Zhao, D. Zhan, X. Zhu, In situ electropolymerized 3D microporous cobalt-porphyrin nanofilm for highly effective molecular electrocatalytic reduction of carbon dioxide, Adv. Mater. 35 (2023) 2303179, https://doi.org/10.1002/adma.202303179.

[4] J. Zhang, Y. Ma, Y. Sun, Y. Zhu, L. Wang, F. Lin, Y. Ma, W. Ji, Y. Li, L. Wang, Enhancing deep mineralization of refractory benzotriazole via carbon nanotubes-intercalated cobalt copper bimetallic oxide nanosheets activated peroxymonosulfate process: mechanism, degradation pathway and toxicity, J. Colloid Interface Sci. 628 (2022) 448–462, https://doi.org/10.1016/j.jcis.2022.07.162.

[5] X. Du, X. Ren, C. Xu, H. Chen, Recent advances on the manganese cobalt oxides as electrode materials for supercapacitor applications: a comprehensive review, J. Energy Storage 68 (2023) 107672, https://doi.org/10.1016/j.est.2023.107672.

[6] J.H. Jun, J. Paeng, J. Kim, J. Shin, I.-S. Choi, J.-H. Lee, Intertwined CNT assemblies as an all-around current collector for volume-efficient lithium-ion hybrid capacitors, ACS Appl. Mater. Interfaces 15 (2023) 25484–25494. https://10.1021/acsami.3c02492.

[7] C. Wang, M. Yuan, W. Shi, X. Liu, L. Wu, Z.-Y. Hu, L. Chen, Y. Li, B.-L. Su, Chelation-Assisted formation of carbon nanotubes interconnected Yolk-Shell Silicon/Carbon anodes for High-Performance Lithium-ion batteries, J. Colloid Interface Sci. 641 (2023) 747–757, https://doi.org/10.1016/j.jcis.2023.03.100.

[8] N. Chamidah, A. Suzuki, T. Shimizu, C. Zhong, K. Shimoda, K.-i. Okazaki, T. Yaji, K. Nakanishi, M. Nishijima, H. Kinoshita, Y. Orikasa, Kinetic analysis of silicon–lithium alloying reaction in silicon single crystal using soft X-ray absorption spectroscopy, RSC Adv. 13 (2023) 17114–17120. https://10.1039/D3RA02554C.

[9] X. Meng, J. Wang, L. Li, Layered-oxide cathode materials for fast-charging lithium-ion batteries: a review, in: Molecules vol. 28, 2023.

[10] L. Li, S. Jia, Z. Cheng, C. Zhang, Improved strategies for separators in zinc-ion batteries, ChemSusChem 16 (2023) e202202330, https://doi.org/10.1002/cssc.202202330.

[11] P. Ma, Z. Zhuang, J. Cao, B. Ju, X. Xi, ZnO–CoO composite nanosphere array-modified carbon cloth for low-voltage hysteresis Li metal anodes, ACS Appl. Energy Mater. 5 (2022) 6417–6422. https://10.1021/acsaem.2c00860.

[12] M. Sun, H. Zhang, Y.-F. Wang, W.-L. Liu, M.-M. Ren, F.-G. Kong, S.-J. Wang, X.-Q. Wang, X.-L. Duan, S.-Z. Ge, Co/CoO@N-C nanocomposites as high-performance anodes for lithium-ion batteries, J. Alloys Compd. 771 (2019) 290–296. https://doi.org/10.1016/j.jallcom.2018.08.312.

[13] H. Qiu, H. Zheng, Y. Jin, Q. Yuan, X. Zhang, C. Zhao, H. Wang, M. Jia, Mesoporous cubic SnO2-CoO nanoparticles deposited on graphene as anode materials for sodium ion batteries, J. Alloys Compd. 874 (2021) 159967, https://doi.org/10.1016/j.jallcom.2021.159967.

[14] M. Ren, F. Li, W. Liu, M. Li, G. Li, J. Hei, L. Su, L. Wang, CoO@N-Doped carbon composite nanotubes as excellent anodes for lithium-ion batteries, Chemelectrochem 4 (2017) 2862–2869, https://doi.org/10.1002/celc.201700694.

[15] X. Li, Q. Chu, M. Song, C. Chen, Y. Li, X. Tian, Y. Cui, D. Zhao, Porous CoO/Co3O4 nanoribbons as a superior performance anode material for lithium-ion batteries, Appl. Surf. Sci. 618 (2023) 156658, https://doi.org/10.1016/j.apsusc.2023.156658.

[16] J. Jiang, C. Ma, T. Ma, J. Zhu, J. Liu, G. Yang, Y. Yang, A novel CoO hierarchical morphologies on carbon nanofiber for improved reversibility as binder-free anodes in lithium/sodium ion batteries, J. Alloys Compd. 794 (2019) 385–395, https://doi.org/10.1016/j.jallcom.2019.04.275.

[17] Y. Chen, J. Song, Y. Li, Q. Tian, J. Chen, L. Yang, High lithium storage performance of CoO with a distinctive dual-carbon-confined nanoarchitecture, Nanoscale 13 (2021) 12938–12950. https://10.1039/D1NR02523F.

[18] Y. Kong, Y. Luo, Y. Ma, J. Tang, Y. Huang, M. Zhou, S. Han, Pomegranate clusters of N-doped carbon-coated CoOx supported on graphene as a flexible lithium-ion battery anode, ACS Appl. Energy Mater. 5 (2022) 5010–5017. https://10.1021/acsaem.2c00388.

[19] H. Chen, S. Zhang, S. Wu, K. Wang, C. Chen, Y. Chen, W. Chu, Z. Chen, H. Li, H. Liu, Design and synthesis of cellulose nanofiber-derived CoO/Co/C two-dimensional nanosheet toward enhanced and stable lithium storage, J. Colloid Interface Sci. 625 (2022) 915–924, https://doi.org/10.1016/j.jcis.2022.06.092.

[20] R. Sui, G. Zan, M. Wen, W. Li, Z. Liu, Q. Wu, Y. Fu, Dual carbon design strategy for anodes of sodium-ion battery: mesoporous CoS2/CoO on open framework carbon-spheres with rGO encapsulating, ACS Appl. Mater. Interfaces 14 (2022) 28004–28013. https://10.1021/acsami.2c06551.

[21] H. Younes, M.M. Rahman, H. Hong, M. AlNahyan, F. Ravaux, Capacitive deionization performance of asymmetric nanoengineered CoFe2O4 carbon nanomaterials composite, Environ. Sci. Pollut. Control Ser. 30 (2023) 32539–32549. https://10.1007/s11356-022-24516-1.

[22] W. Yuan, J. Zhang, D. Xie, Z. Dong, Q. Su, G. Du, Porous CoO/C polyhedra as anode material for Li-ion batteries, Electrochim. Acta 108 (2013) 506–511. https://10.1016/j.electacta.2013.07.003.

[23] C. Kim, H.-J. Cho, K.R. Yoon, J.Y. Cheong, S.-H. Cho, J.-W. Jung, S.W. Song, I.-D. Kim, Synergistic interactions of different electroactive components for superior lithium storage performance, ACS Appl. Mater. Interfaces 13 (2021) 587–596. https://10.1021/acsami.0c18438.

[24] S. Chen, D. Wu, W. Li, F. Ding, Q. Kang, Y. Li, Capillary phenomena in tubes under microgravity, Braz. J. Phys. 53 (2023) 135. https://10.1007/s13538-023-01328-3.

[25] D. Wang, P. Yang, Y. Hu, Z. Cui, Z. Du, P. Yang, S. Yi, J. Rao, Y. Zhang, 1D-3D biological template loaded NiCo nanowires at high temperatures as a broadband, lightweight electromagnetic wave absorbing material, Powder Technol. 426 (2023) 118670, https://doi.org/10.1016/j.powtec.2023.118670.

[26] J. Chen, Y. Huang, J. liu, C. Li, H. Zheng, X. Xu, L. Fu, X. Li, M. Wang, Y. Lin, H. Cao, Three-dimensional porous Na4MnV(PO4)3 constructed by Aspergillus Niger biological template as a high performance cathode for sodium ion batteries, Electrochim. Acta 458 (2023) 142521, https://doi.org/10.1016/j.electacta.2023.142521.

[27] S. Pothaya, C. Poochai, N. Tammanoon, Y. Chuminjak, T. Kongthong, T. Lomas, C. Sriprachuabwong, A. Tuantranont, Bamboo-derived hard carbon/carbon nanotube composites as anode material for long-life sodium-ion batteries with high charge/discharge capacities, Rare Met. 43 (2024) 124–137. https://10.1007/s12598-023-02414-w.

[28] A. Liu, T.-F. Liu, H.-D. Yuan, Y. Wang, Y.-J. Liu, J.-M. Luo, J.-W. Nai, X.-Y. Tao, A review of biomass-derived carbon materials for lithium metal anodes, N. Carbon Mater. 37 (2022) 658–674, https://doi.org/10.1016/S1872-5805(22)60620-6.

[29] Y. Chen, Y. Wu, Y. Liao, Z. Zhang, S. Luo, L. Li, Y. Wu, Y. Qing, Tuning carbonized wood fiber via sacrificial template-assisted hydrothermal synthesis for high-performance lithium/sodium-ion batteries, J. Power Sources 546 (2022) 231993, https://doi.org/10.1016/j.jpowsour.2022.231993.

[30] L. Pei, H. Cao, L. Yang, P. Liu, M. Zhao, B. Xu, J. Guo, Hard carbon derived from waste tea biomass as high-performance anode material for sodium-ion batteries, Ionics 26 (2020) 5535–5542. https://10.1007/s11581-020-03723-1.

[31] M. Mohseni, D. Felder, K. Percin, M. Thönes, M. Gassenmeier, R. Kupec, C. Weidlich, J. Linkhorst, R.G. Keller, M. Wessling, Toward decentralized wastewater treatment: a flow-through module using microtubular gas diffusion electrodes for micropollutants removal, J. Hazard Mater. 458 (2023) 131987, https://doi.org/10.1016/j.jhazmat.2023.131987.

[32] B. Wang, F. Yang, L. Feng, Recent advances in Co-based electrocatalysts for hydrogen evolution reaction, Small 19 (2023) 2302866, https://doi.org/10.1002/smll.202302866.

[33] G. Sun, R. Gao, H. Jiao, D. Luo, Y. Wang, Z. Zhang, W. Lu, M. Feng, Z. Chen, Self-Formation CoO nanodots catalyst in Co(TFSI)2-Modified electrolyte for high efficient Li-O2 batteries, Adv. Mater. 34 (2022) 2201838, https://doi.org/10.1002/adma.202201838.

[34] Y. Wang, D. Xu, X. Zhang, X. Hong, G. Liu, Selective C2+ alcohol synthesis by CO2 hydrogenation via a reaction-coupling strategy, Catal. Sci. Technol. 12 (2022) 1539–1550. https://10.1039/D1CY02196F.

[35] S. Ye, Y. Zhang, W. Xiong, T. Xu, P. Liao, P. Zhang, X. Ren, C. He, L. Zheng, X. Ouyang, Q. Zhang, J. Liu, Construction of tetrahedral CoO4 vacancies for activating the high oxygen evolution activity of Co3−xO4−δ porous nanosheet arrays, Nanoscale 12 (2020) 11079–11087. https://10.1039/D0NR00744G.

[36] S. Debnath, A. Das, R. Das, Effect of cobalt doping on structural parameters, cation distribution and magnetic properties of nickel ferrite nanocrystals, Ceram. Int. 47 (2021) 16467–16482, https://doi.org/10.1016/j.ceramint.2021.02.095.

[37] D. Wang, Z. Zhao, B. Shi, J.-X. Wang, J.-F. Chen, Real-time imaging and quantitative evolution for pyrolysis of carbon dots-encapsulated metal–organic frameworks at the nanoscale by in situ environmental transmission electron microscopy, ACS Appl. Mater. Interfaces 15 (2023) 35358–35365. https://10.1021/acsami.3c05715.

[38] M.J. Giannetto, E.P. Johnson, A. Watson, E. Dimitrov, A. Kurth, W. Shi, F. Fornasiero, E.R. Meshot, D.L. Plata, Modifying the molecular structure of carbon nanotubes through gas-phase reactants, ACS Nanoscience Au 3 (2023) 182–191. https://10.1021/acsnanoscienceau.2c00052.

[39] X. Sun, P. Wang, K. Davey, Y. Zheng, S.-Z. Qiao, Mild methane electrochemical oxidation boosted via plasma pre-activation, Small 19 (2023) 2303428, https://doi.org/10.1002/smll.202303428.

[40] X. Yao, Y. Zhu, T. Xia, Z. Han, C. Du, L. Yang, J. Tian, X. Ma, J. Hou, C. Cao, Tuning carbon defect in copper single-atom catalysts for efficient oxygen reduction, Small 19 (2023) 2301075, https://doi.org/10.1002/smll.202301075.

[41] C. Jiang, X. Chang, X. Wang, Z.-J. Zhao, J. Gong, Enhanced C–H bond activation by tuning the local environment of surface lattice oxygen of MoO3, Chem. Sci. 13 (2022) 7468–7474. https://10.1039/D2SC01658C.

[42] K. Choi, S. Kim, Theoretical study of oxygen reduction reaction mechanism in metal-free carbon materials: defects, structural flexibility, and chemical reaction, ACS Nano 16 (2022) 16394–16401. https://10.1021/acsnano.2c05607.

[43] Z. Dong, D.W.C. MacMillan, Metallaphotoredox-enabled deoxygenative arylation of alcohols, Nature 598 (2021) 451–456. https://10.1038/s41586-021-03920-6.

[44] C.P. Sandhya, B. John, C. Gouri, Synthesis, characterization and electrochemical evaluation of mixed oxides of nickel and cobalt from spent lithium-ion cells, RSC Adv. 6 (2016) 114192–114197. https://10.1039/c6ra22439c.

[45] C.P. Sandhya, B. John, C. Gouri, H. Sreemoolanadhan, S.K. Manwatkar, Promising anode material for lithium-ion cells based on cobalt oxide synthesized by microwave heating, Ionics 23 (2017) 1693–1701. https://10.1007/s11581-017-2015-z.